






# Towards Resiliency Enhancement of Network of Grid-Forming and Grid-Following Inverters

Silvanus D'silva , *Student Member, IEEE*, Alireza Zare , *Student Member, IEEE*,  
 Mohammad B. Shadmand , *Senior Member, IEEE*, Sertac Bayhan , *Senior Member, IEEE*,  
 and Haitham Abu-Rub , *Fellow, IEEE*

**Abstract**—This article proposes an autonomous control scheme to mitigate voltage–frequency excursions observed in a network of grid-forming (GFM) and grid-following (GFL) inverters in a power-electronics-dominated grid (PEDG). The proposed control scheme leverages the GFL inverter's ability to dynamically adjust their power set-points as well as change their operation mode on-the-fly to enhance the PEDG resiliency. A supervisory controller comprising of a droop- $\Delta P$  estimator coupled with an optimal power allocator module dynamically adjusts the power injections from GFL inverters to maintain the power balance and restore frequency in response to disturbances. Moreover, the proposed self-ranking-based coordinated mode selection algorithm dynamically reconfigures the inverter's operation mode (either GFM or GFL) to enhance the PEDG resiliency in response to events and ensure GFM inverter allocation in grid clusters. Several case studies are performed to validate the feasibility, performance, and robustness of the proposed autonomous control. Finally, the proposed scheme is experimentally validated on a small-scale hardware testbed.

**Index Terms**—Frequency restoration, grid-following (GFL) inverter, grid-forming (GFM) inverter, resiliency.

## I. INTRODUCTION

CURRENT trend towards the integration of renewable sources in the power system, backed by the net-zero emissions goal of several governmental agencies, have led to the emergence of a power-electronics-dominated grid (PEDG)

Manuscript received 7 November 2022; revised 30 January 2023; accepted 16 March 2023. Date of publication 3 April 2023; date of current version 16 August 2023. This work was supported by the Qatar National Research Fund (QNRF is a member of Qatar Foundation) under Grants NPRP12C-33905-SP-213 and NPRP12C-33905-SP-220. The statements made herein are solely the responsibility of the authors. (Corresponding author: Mohammad B. Shadmand.)

Silvanus D'silva, Alireza Zare, and Mohammad B. Shadmand are with the Department of Electrical & Computer Engineering, University of Illinois Chicago, Chicago, IL 60607 USA (e-mail: sdsilv2@uic.edu; azare2@uic.edu; shadmand@uic.edu).

Sertac Bayhan is with the Qatar Environmental and Energy Research Institute, Hamad Bin Khalifa University, Doha 34110, Qatar, and also with the Department of Electrical-Electronic Engineering, Technology Faculty, Gazi University, Ankara, Turkey (e-mail: sbayhan@hbku.edu.qa; sbayhan@gazi.edu.tr).

Haitham Abu-Rub is with the Electrical and Computer Engineering Department, Texas A&M University at Qatar, Doha 23874, Qatar (e-mail: haitham.abu-rub@qatar.tamu.edu).

Color versions of one or more figures in this article are available at <https://doi.org/10.1109/TIE.2023.3262866>.

Digital Object Identifier 10.1109/TIE.2023.3262866

paradigm [1]. PEDG aims at transforming the conventional grid into an intricate network of inverter-based resources [2]. A typical PEDG is characterized by generation units located in close proximity to loads, uninterrupted power fed to local loads enhancing the system's resiliency, dynamic islanding and reconnection abilities via multiple points of common coupling (PCC), inverter-based voltage–frequency ( $V$ - $f$ ) restoration, etc. [3], [4]. On the contrary, PEDG has also introduced multiple challenges, such as inherent lower inertia due to the replacement of synchronous generators with inverters, the need for complex multilayered multi-timescale controllers, weather-related generation constraints, a lower reactance-to-resistance ( $X/R$ ) ratio, and lower fault ride-through capabilities [1]. Besides, the transformation from centralized to distributed generation has also compromised the PEDG's security and made it vulnerable to potential anomalies [3], [4].

The resilient operation of PEDG is highly dependent upon distributed energy resources (DERs), which are interfaced with the grid via inverters. The inverters in a PEDG are commonly operated in either 1) grid-forming (GFM) or 2) grid-following (GFL) modes. A GFM inverter is characterized by a controlled voltage source that regulates its output  $V$ - $f$ , whereas a GFL inverter is characterized by a controlled current source that injects the desired amount of active–reactive power when demanded by the network. The optimal dispatch set-points of GFL inverters are typically obtained from a supervisory controller (SC) [3], [4]. On the other hand, GFM inverters support the  $V$ - $f$  in the PEDG and typically provide virtual inertia to enhance the system's resiliency. Multiple studies have been carried out in the literature to investigate the enhancement of  $V$ - $f$  dynamic response by selecting the proper mode of inverter operation, i.e., GFM versus GFL mode. The strategic placement of GFM and GFL inverters enhances the  $V$ - $f$  dynamic response, demand–supply stability, and the inertial response of the PEDG [5]. Various studies have also explored the fact that advanced functions such as damping [6] and virtual inertia emulation [7] via a fleet of GFM inverters enhance the system's stability. However, a PEDG network containing 100% GFM inverters may introduce its own set of challenges related to synchronization, circulating reactive powers, unregulated power sharing, etc., as each GFM tries to regulate the network's  $V$ - $f$  [8]. On the contrary, at least one GFM inverter is essential in each cluster in PEDG, with the islanding capability to maintain slack bus crucial for synchronization of GFL inverters within the cluster boundaries and ensure required

inertia emulation. This article considers a PEDG islanded cluster with at least one GFM inverter interacting with several GFL inverters controlled by a multilayered, multi-timescale control scheme towards enhancing the resiliency of the network.

Various control approaches for the network of GFM and GFL inverters in PEDG have been proposed in the literature and are mainly classified as centralized and distributed control schemes [3], [9], [10], which can mitigate disturbance impacts to some extent. In the centralized control approach, the satisfactory operation of the PEDG clusters heavily relies on a central SC, which provides adequate power references to inverters along with vital protection features in the grid-connected and islanded modes [11], [12]. Various primary controllers for GFM and GFL inverters, such as droop-based, virtual-synchronous-generator-based, and virtual-oscillator-control-based schemes, are deployed in a centralized control architecture where the SC provides the active–reactive power setpoints to these inverter’s primary controllers to maintain system stability. However, in general, the centralized control approach suffers from an inherent drawback related to a single point of failure. Alternatively, distributed control approaches have been proposed in [13] where each inverter is equipped with a local coordinated controller in addition to the primary voltage or current controller, thereby eliminating SC’s dependency. Each inverter that could be modeled as an agent interacts with its neighbors in a coordinated manner to attain the desired control objective. However, since agents only communicate with their neighbors, limited information about the entire cluster is available, which limits their performance compared to centralized schemes [14], [15], [16], [17]. In summary, the above-mentioned control approaches adjust the GFL inverters’ operation setpoints in a centralized or distributed manner to address the  $V$ - $f$  fluctuations, provided all resources in the PEDG are available.

The missing piece of the puzzle here is what if an intentional or unintentional disturbance targets the PEDG resources, typically the GFM and GFL inverters. This article aims at addressing this research gap to ensure the resilient operation of PEDG clusters against  $V$ - $f$  related disturbances. In a PEDG, such disturbances may arise due to a variety of reasons, such as undesirable loss of load, generation loss due to insufficient incident solar irradiation, depleted state of charge (SoC) and state of health of coupled battery energy storages (BESS) [18], [19], and power stage failures, thereby leading to a power demand–supply imbalance. Furthermore, disturbances may also be introduced due to compromised or faulted GFM and GFL inverter controllers. Thus, a real-time fault-resilient mechanism that can mitigate the catastrophic impacts of disturbances in the PEDGs  $V$ - $f$  is required. This article aims at addressing the associated  $V$ - $f$  fluctuations regardless of the cause such as the loss of the GFM or GFL inverter.

The proposed solution is based on an integrated centralized and distributed control framework that leverages the features of these two classes of control architecture for a more resilient operation of the PEDG. Subsequently, this article proposes a real-time autonomous control to restore the  $V$ - $f$  in an islanded PEDG cluster consisting of one GFM inverter and multiple GFL inverters. The proposed approach uses a self-ranking-based

coordinated mode selection (SR-CMS) mechanism capable of dynamically reconfiguring the inverter’s operation mode to restore the PEDG and feed uninterrupted power to critical loads. Thus, the key contributions of this article are as follows:

- 1) an integrated centralized and distributed control scheme for more resilient operation of PEDG,
- 2) real-time estimation of demanded power “ $\Delta P$ ” and optimal power allocation among inverters to restore frequency,
- 3) self-reconfiguration of inverters’ operation modes within the cluster in response to the loss of GFM inverters arising from failure of the source, controller, power stage, etc.,
- 4) accurate power sharing among inverters, thereby eliminating periodic reconfiguration of droop gains.

Furthermore, the superiority of the proposed control architecture is also compared with state-of-the-art droop-based control schemes. Table I shows the features and drawbacks of the state-of-the-art control schemes for a network of GFM and GFL inverters in PEDG and compared them with the proposed SR-CMS-based control scheme. These distributed control schemes can be categorized into GFM only [20], [21], [22], [23] or a combination of GFM and GFL inverters [5], [13], as summarized in Table I. The rest of this article is structured as follows. Section II describes the PEDG and its various components, along with the inverter’s proposed controller architecture. Section III discusses the proposed SC comprising droop- $\Delta P$  estimation module and an optimal power allocator (OPA) module. The proposed packet generation and coordinated mode selection mechanism is also discussed in this section. Section IV explains the simulation case studies’ results. The results obtained from experimental hardware validation of the proposed SR-CMS scheme on a small-scale testbed comprising three inverters are discussed in Section V. Finally, Section VI concludes this article.

## II. SYSTEM OVERVIEW

### A. System Description

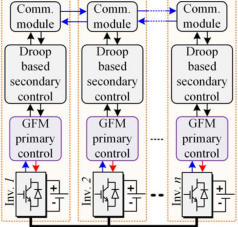
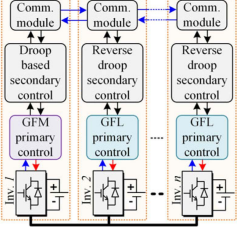
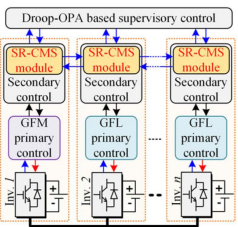
The architecture of the proposed islanded grid clusters in the PEDG is depicted in Fig. 1. The string inverters are connected at the cluster’s PCC. The considered PEDG is divided into “ $n$ ” clusters, each containing “ $z$ ” string inverters that have dual operation modes and are capable of switching between modes when demanded. Each string comprises a source-connected converter (SCC) cascaded with a grid-connected dc–ac inverter (GCI), each equipped with its independent primary controllers, as discussed in [24]. A cluster coordinated controller (CCC) governs the cluster’s operation and serves as a local power dispatcher when the SC is faulted or compromised.

### B. Grid-Connected Inverter

A detailed description of the GCI that interfaces the hybrid dc source to the PCC is provided in [24]. As shown in Fig. 1(b), each GCI is driven by a model predictive controller that uses the  $LCL$  filter’s dynamic model [25] to minimize the cost function “ $g$ .” The controller’s cost function “ $g$ ” is given as follows:

$$g = \Gamma_i |v_{\text{pcc}}^* - v_{\text{pcc},k+1}| + (1 - \Gamma_i) |i_g^* - i_{g,k+1}| \quad (1)$$

TABLE I  
COMPARISON OF STATE-OF-THE-ART CONTROL SCHEMES FOR RESILIENT OPERATION OF GFM AND GFL INVERTERS IN A PEDG

Method	Topology	Features	Drawbacks
Multiple Droop-based GFM-only cluster [20], [21], [22], [23]		<ul style="list-style-type: none"> <li>Minimal or no dependency on communication layer.</li> <li>High modularity, flexibility, and expandability.</li> <li>Virtual inertial emulation capability.</li> </ul>	<ul style="list-style-type: none"> <li>Multiple droop gain tuning challenges.</li> <li>Synchronization of multiple GFM inverters is challenging.</li> <li>Vulnerability to steep load disturbance due to lack of sufficient coordination.</li> <li>Dependency on communication links for synchronization, adaptiveness, etc.</li> <li>Can be implemented without communication in decentralized scheme at the cost of improper power sharing.</li> </ul>
Single droop-based GFM and multiple GFL-based cluster [5], [13]		<ul style="list-style-type: none"> <li>Simple synchronization between single GFM and multiple GFL inverters.</li> <li>Generation and load disturbances can be compensated by GFM and GFL inverters at different time scales.</li> <li>In case of a GFL failure, GFM and other GFLs can adjust their power set point to maintain power balance.</li> </ul>	<ul style="list-style-type: none"> <li>Vulnerable to single point of failure.</li> <li>Failure or compromised GFM inverter will result in loss of slack bus and PCC V-f regulation is lost.</li> <li>Lack of coordination between reverse-droop based GFLs and without considering their power reserve may result in fluctuations in V-f in response to disturbances.</li> <li>Communication dependency.</li> <li>No self-healing capability.</li> </ul>
Proposed SR-CMS-based GFM-GFL-cluster		<ul style="list-style-type: none"> <li>Resilient to GFM failure or other single point of failures.</li> <li>Simple synchronization between GFM and GFL inverters.</li> <li>Optimal power sharing between all DERs considering their power reserve.</li> <li>Minimal tuning effort for droop gains by minimizing the number of droop curves within the cluster.</li> <li>Self-healing capability for determining the optimal next GFM candidate in response to failures.</li> <li>Maximum resiliency and robustness with minimal communication requirement.</li> </ul>	<ul style="list-style-type: none"> <li>Communication dependency.</li> </ul>

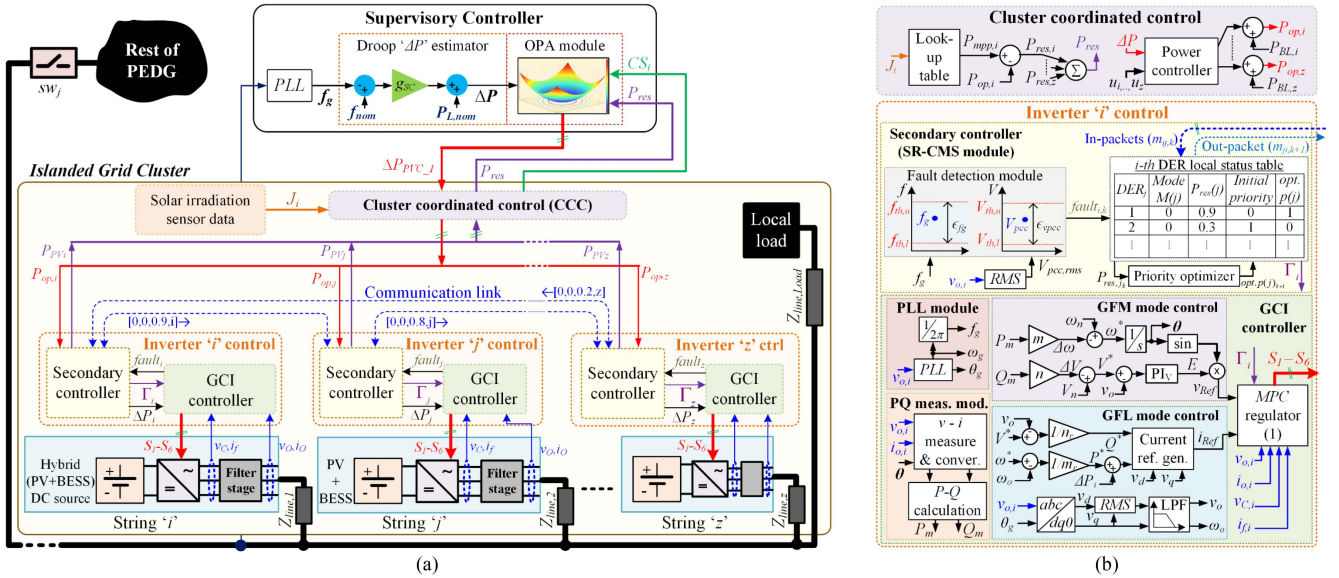


Fig. 1. Proposed SR-CMS control scheme for an islanded grid cluster. (a) Proposed system architecture. (b) Inverter controllers.

where  $v_{pcc}^*$  and  $i_g^*$  indicate the output voltage's and grid current's reference values, respectively, and  $v_{pcc,k+1}$  and  $i_{g,k+1}$  correspond to the next step's predicted values for output voltage and grid current, respectively. Next,  $\Gamma_i$  is a binary factor that determines the GCI's operation mode. In the GFM mode,  $\Gamma_i$  is set to "1," and the GCI operates as a controlled voltage source,

whereas in the GFL operation,  $\Gamma_i$  is set to "0," and the GCI operates in the current-controlled mode regulated by SC. Since the grid impedance in a PEDG is neither purely resistive nor inductive, the active and reactive power droop relations are not fully decoupled either. Thus, modified droop relations [26] that generate references for the GFM operation are given as



follows:

$$f_g - f_0 = m_p (P - P_0) + n_q (Q - Q_0) \quad (2)$$

$$v_g - v_0 = m_p (P - P_0) - n_q (Q - Q_0) \quad (3)$$

where  $f_g$  and  $v_g$  represent the measured frequency and PCC voltage, respectively, and  $f_0$  and  $v_0$  represent the nominal frequency and voltage, respectively.  $m_p = k_p (X_{\text{line}}/Z_{\text{line}})$  and  $n_q = k_q (R_{\text{line}}/Z_{\text{line}})$  are the effective frequency and voltage droop gains, respectively. The droop gains depend on the ratio of resistive  $R_{\text{line}}$  and inductive line impedances  $X_{\text{line}}$  between two strings and  $Z_{\text{line}} = \sqrt{R_{\text{line}}^2 + X_{\text{line}}^2}$ .  $P_0$  and  $Q_0$  represent the active and reactive powers of GCI in GFM, respectively. Also,  $P = P_m(\omega_c/(s + \omega_c))$  and  $Q = Q_m(\omega_c/(s + \omega_c))$  are the measured active–reactive powers passed through a low-pass filter of cut-off frequency  $\omega_c$ .

### C. Cluster Coordinated Control

The CCC acts as the moderator between the SC and the SCC and GCI primary controllers. It determines the available power reserve in its strings based on the power output and the estimated maximum power and conveys the total power reserve level to the SC. The maximum power is estimated using look-up tables using solar irradiation inputs given by  $P_{\text{mpp},s} = f(J_s)$ . Here,  $f(J_s)$  represents the look-up function discussed in [24]. Since all strings in a cluster are located nearby, the estimated  $P_{\text{mpp},s}$  coincides with the maximum generation ability. The instantaneous power reserve  $P_{\text{res}}$  in a cluster is given as follows:

$$P_{\text{res}} = \sum_{s=1}^z (P_{\text{mpp},s} - P_{\text{op},s}) \quad (4)$$

where  $P_{\text{op},s}$  is the  $s$ -th string output power. This value of  $P_{\text{res}}$  is sent to the SC to determine the next instance demanded power  $\Delta P$ , as discussed in Section III. Also, it assigns the power demand obtained from the SC to all connected strings. Thus, at any instance, the output power of a string  $s$  is given as base load  $P_{\text{BL},s}$  plus allocated demand  $\Delta P_s$  in  $P_s = P_{\text{BL},s} + u * \Delta P_s$ . Here,  $u$  is a binary operator set to “0” if string  $s$  is operating in GFM or is faulted; else, it is set to “1” for GFL operation. Thus, the cluster’s total harvested power  $P_k$  at instance  $k$  is given as follows:

$$P_k = \sum_{s=1}^z P_{s,k} = \sum_{s=1}^z (P_{\text{BL},s,k} + (u^* \Delta P_{s,k})). \quad (5)$$

## III. PROPOSED CONTROL SCHEME

### A. $\Delta P$ Estimator and OPA

A droop-based  $\Delta P$  estimator coupled with the OPA module in the SC is deployed to restore the frequency in a timely manner, particularly during load disturbances. The  $\Delta P$  estimator determines the demanded power to maintain frequency  $f_g$  by

$$\Delta P = P_0 - P_g = g_{\text{SC}} (f_g - f_0) \quad (6)$$

where  $\Delta P$  is the differential power required to restore the frequency  $f_g$  to nominal  $f_0$ .  $P_0$  is the nominal load, and  $P_g$  is the PEDG’s currently served load. Also,  $g_{\text{SC}}$  is the SC’s gain.

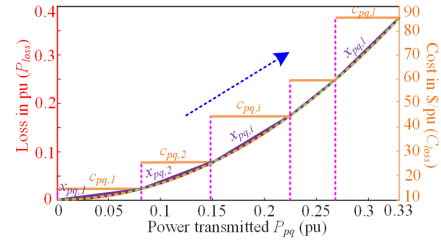


Fig. 2. Power transferred between strings  $p$  and  $q$  versus power loss versus loss cost.

The OPA module uses a convex-optimization-based linear programming (LP) module to minimize power loss through incurred loss cost while ensuring system stability. A detailed analysis of the OPA module is provided in [24]. Consequently, the power loss incurred during power transfer from string  $p$  to string  $q$  is given by the red curve in Fig. 2, which is translated to a loss cost curve represented by the dotted green curve. For ease in formulation, power transferred from string  $p$  to string  $q$  is approximated by the linear piecewise function of  $l$  segments bearing generation rate  $x_{pq,i}$ . This function is represented by the purple plot. Thus, equality constraints for LP are given as follows:

$$\Delta P_{pq} = \sum_{i=1}^l x_{pq,i} ; i = (1, 2, \dots, l) ; q = (1, 2, \dots, z). \quad (7)$$

Also, the lower limit and higher limits  $X_{pq,i}^{\text{max}}$  for all  $l$  segments provide the inequality constraints given as follows:

$$0 \leq x_{pq,i} \leq X_{pq,i}^{\text{max}} ; i = (1, 2, \dots, l). \quad (8)$$

Next, a cost factor  $c_{pq,i}$  is assigned to each segment, illustrated by the horizontal orange segments in Fig. 2. The values assigned to  $c_{pq,i}$  depend on the line impedances, loading profiles, etc. The generation uncertainties are incorporated into the cost function using a factor  $b_{pq,i}$  with a value ranging from 0.0 to 1.0 depending on incident solar irradiation. The power constraints that converge the system are given as follows:

$$\Delta P_p = \sum_{q=1}^z \Delta P_{pq}. \quad (9)$$

Finally, the cost function  $\Phi_p$  that is to be minimized is expressed as the summation of the product of segment generations, cost factors, and uncertainty factor  $b_{pq,i}$  given as follows

$$\Phi_p = \min \{C_{\text{loss},p}\} = \min \left\{ \left[ \sum_{q=1}^z \left( \sum_{i=1}^l c_{pq,i} b_{pq,i} x_{pq,i} \right) \right] \right\} \quad (10)$$

The OPA module minimizes (10) using (11) shown at the bottom of the next page, to determine the next instance optimal power allocations to GFL inverters, in response to assigned  $\Delta P$  by following the flowchart shown in Fig. 3.



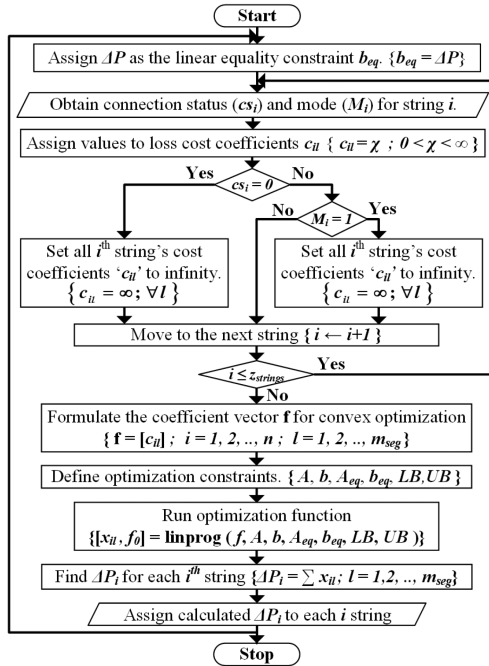


Fig. 3. Flowchart illustrating the execution of the OPA module.

## B. Proposed SR-CMS Control

The proposed SR-CMS control scheme uses a meshed communication network to enhance the resiliency of the PEDG against an inverter's faulted controller or intentional disturbances. This meshed communication network is indicated by the blue dashed lines connecting each string inverter with its neighbors in Fig. 1(a). Each string inverter is considered a member agent and is modeled as a node. It is worth noting that the terms "inverter" and "agent" are interchangeably used here. In the event of a faulted GFM agent's controller, its power stage is disconnected from the PCC. However, this causes loss of PCC  $V$ - $f$  references essential for the GFL agents and system loads. To avoid this, the SR-CMS mechanism is deployed on each agent's secondary controller. This mechanism exchanges status update packets between all neighboring agents to dynamically elect the next GFM inverter, as discussed below.

## C. Proposed SR-CMS Mechanism: Packet Generation

To facilitate network visibility, a status update packet  $m_{ij}$  is produced by agent "j" and shared to all its neighbors

$$m_{ij} = [f_j, M_j, P_{res,j}, \text{opt}.p_j]. \quad (12)$$

Here, (12) represents the status update packet shared by agent  $j$  with every neighboring agent  $i$ .  $f_j$  denotes agent  $j$ 's fault status, which is set to 1 if a fault is detected at its PCC. The  $M_j$  bit indicates  $j$ 's operation mode, in GFM ( $M_j = 1$ ) or GFL ( $M_j = 0$ ). Next,  $P_{res,j}$  signifies the available power reserve in terms of a percentage of the agent  $j$ 's total capacity. This value is regulated by agent  $j$ 's primary controller and depends on the available power reserve in the hybrid dc source bound by the operation set-point, maximum available power, BESS's SoC, etc. Finally, "opt. $p_j$ " field represents the global optimized priority, which is determined by a consensus between all agents. The consensus procedure is explained in the following sub-section. During an event, the agent with " $P_{res,j}$ " matching the "opt. $p_j$ " in its local status table is elected as the next GFM.

## D. Proposed SR-CMS: Rank-Based Mechanism

Fig. 4 shows a graphical representation of the cluster, consisting of one GFM and four GFL inverters. To maintain stable operation when a GFM fails, the rank-based approach is deployed. Consider  $N$  agents in a cluster. An initial rank  $R_{0,i}$  is assigned to the agents based on their available power reserve so that each agent has a unique identification number given by

$$R_{0,i} = (id)_i N; \quad i = (1, \dots, 5); \quad N = (1, \dots, i). \quad (13)$$

Here,  $i$  represents the total number of available agents, and  $N$  indicates the number of integers required for initial rankings. As discussed previously, all communications among agents occur through exchanged packets. For a faulted GFM  $j$ , as the error between PCC voltage magnitude  $V_{pcc}$  and threshold  $V_{pcc,th}$  crosses tolerance  $\varepsilon_{vpcc}$  and as the error between frequency  $f_g$  and threshold  $f_{g,th}$  crosses tolerance  $\varepsilon_{fg}$ ,  $f_i$  bit is set to 1 as follows:

$$\begin{aligned} \text{err}(V_{pcc}) &= |V_{pcc} - V_{pcc,th}| \\ &\Rightarrow \begin{cases} f_i = 1 & \text{if } \text{err}(V_{pcc}) > \varepsilon_{vpcc} \\ f_i = 0 & \text{if } \text{err}(V_{pcc}) \leq \varepsilon_{vpcc} \end{cases} \end{aligned} \quad (14)$$

$$\text{err}(f_g) = |f_g - f_{th}| \Rightarrow \begin{cases} f_i = 1 & \text{if } \text{err}(f_g) > \varepsilon_{fg} \\ f_i = 0 & \text{if } \text{err}(f_g) \leq \varepsilon_{fg} \end{cases}. \quad (15)$$

The tolerance values for amplitude  $\varepsilon_{vpcc}$  and frequency  $\varepsilon_{fg}$  are designed by the system operator. The "opt. $p_i$ " in (11) represents the next available agent to take over the GFM role. Equation (16) uses the fault status from (14) and (15), the available power reserve of each agent, and "opt. $p_i$ " at instance " $k - 1$ " to select the most viable candidate inverter as the next GFM agent at

$$C_{loss} = \begin{bmatrix} c_{12,1}b_{12,1}x_{12,1} + c_{12,2}b_{12,2}x_{12,2} + \dots + c_{1z,l}b_{1z,l}x_{1z,l} \\ + \dots \\ + c_{p1,1}b_{p1,1}x_{p1,1} + \dots + c_{pq,l}b_{pq,l}x_{pq,l} + \dots + c_{pz,l}b_{pz,l}x_{pz,l} \\ + \dots \\ + c_{n1,1}b_{n1,1}x_{n1,1} + \dots + c_{nz,l}b_{nz,l}x_{nz,l} \end{bmatrix}. \quad (11)$$

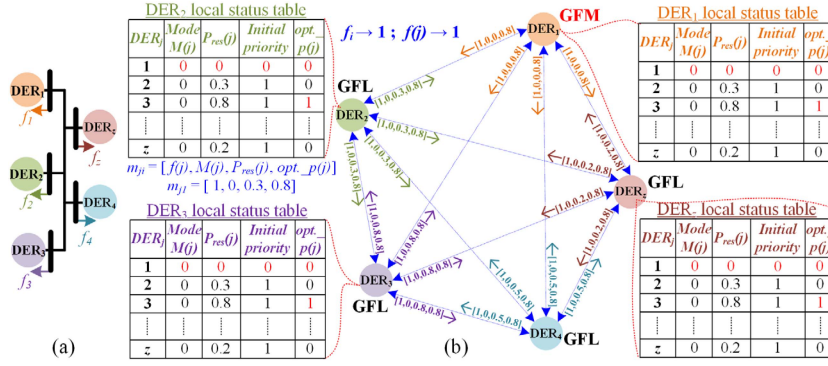


Fig. 4. Proposed SR-CMS mechanism: packet-based coordination between DERs. (a) Power stage. (b) Communication graph.

instance  $k$  via the established priority function as follows:

$$\begin{aligned} \text{opt}.p_{i,k} &= \text{opt}.p_{i,k-1}(1 - f_{i,k-1}) + [\max(P_{res,i,k-1})] f_{i,k-1} \\ M_{i,k} &= \text{prior}_{i,k}(\text{opt}.p_{i,k}). \end{aligned} \quad (16)$$

### E. Proposed SR-CMS Mechanism

The proposed SR-CMS mechanism provides full visibility of the entire cluster to each of its agents. The initialization process assigns initial priorities to each agent based on their generation capacities. Based on the results of the rank-based local optimizer (LO), the GFM agent is elected, whereas other agents operate in GFL. Following the initialization process, each agent in the cluster periodically broadcasts a status update packet to all neighboring agents. The execution flow of the proposed SR-CMS mechanism is illustrated in Fig. 5. Under normal conditions, consider that agent  $j$  is in GFM, whereas other agents operate in the GFL mode with no disturbances in the system. Agent  $j$  broadcasts a status update packet at instance  $k$  as  $m_{ij} = [0, 1, 0.9, 0.9]$ . Here, the packet signifies that agent  $j$  is in GFM and maintains a power reserve of 0.9. Furthermore, it indicates that no fault has been detected at  $j$ 's PCC and "opt. $p_j$ " is 0.9. Accordingly, all neighbors update  $j$  status entry in their local update tables. In response, all neighbors send a status update packet to agent  $j$  with their updated  $P_{res,j}$  and "opt. $P_j$ " values.

When a GFL operating agent " $k$ " fails, the secondary controller disregards its binary factor  $\Gamma_k$  value, sets its connection status " $cs_k$ " to 0, and disconnects it from the PCC. Moreover, the secondary controller also flags the failed GFL " $k$ " by setting its "Initial priority" to 0 and its " $P_{res,k}$ " to 0 to exclude it from the next candidate GFM selection process. This ensures that the next potential GFM candidate is not a faulty GFL agent.

Similarly, when a GFM agent " $j$ " fails, the PCC  $V$ - $f$  limit violation is detected by the fault detection module in the proposed SR-CMS secondary controller. The secondary controller then disregards the value of binary factor  $\Gamma_j$  and disconnects the agent " $j$ " from its PCC. Furthermore, the mode bit  $M_j$  is set to 0 in agent  $j$ 's local status table. Also, "Initial priority" is set to 0, " $P_{res,j}$ " is set to 0 (as evident from the control flow shown in Fig. 5), and "opt. $p_j$ " is updated to the new value obtained from LO (see Fig. 4). Agent ' $j$ ' now broadcasts the updated packet

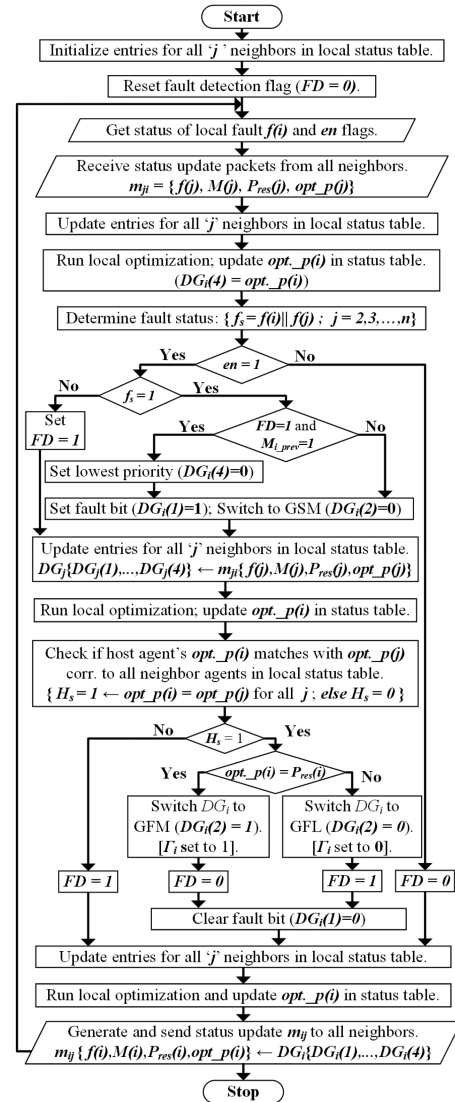


Fig. 5. Flowchart for execution of the proposed SR-CMS algorithm.

$m_{ij} = [1, 0, 0.0, 0.8]$ , conveying its fault status to neighboring agents. The  $f_j$  bit is set to 1 and mode bit  $m_j$  is set to 0, indicating the inability to operate as GFM. Subsequently, all neighboring agents flag the agent  $j$  and run LO to find new  $opt.p_i$ . Agent

TABLE II  
SYSTEM SPECIFICATIONS AND COMPONENT PARAMETERS

Symbol	Parameter	Value
$z$	Strings per cluster	5
$P_{GFM}$	GFM string's max. output power	22.06 kW
$P_{GFL}$	GFL string's max. output power	10.4 kW
$f_{sw}$	SCC's switching frequency	10 kHz
$C_{dcl}$	SCC's output-side capacitance	600 $\mu$ F
$V_{dcl,ref}$	Reference DC-link voltage	650 V
$f_{inv,sw}$	GCI's switching frequency	28 kHz
$L_{in}$	GCI's inverter-side filter inductance	1.3 mH
$C_f$	GCI's filter capacitance	80 $\mu$ F
$R_d$	Filter capacitor's damping resistance	0.1 $\Omega$
$L_g$	Grid-side filter inductance	1 mH
$V_{g,rms}$	RMS grid voltage	208 V
$f_g$	Line frequency	60 Hz

' $j$ ' uses the status update packets received from all neighbors to update its local status table and determine new  $opt.p_i$  as indicated in the control flowchart in Fig. 5. This process of update exchange repeats, and synchronization is complete when all the entries of  $opt.p(j)$  in agent  $j$ 's local status table have the same homogenized priority values. After synchronization is attained, all agents are fully aware of their neighbor's status, and the next eligible candidate takes over as the next GFM. Thus, agents are aware of their neighbor's status.

To elect the next GFM candidate, each agent  $i$  checks if its *Initial priority*( $i$ ) matches the homogenized  $opt.p(i)$ . If the *Initial priority*( $i$ ) matches the  $opt.p(i)$ , agent  $i$ 's binary factor  $\Gamma_i$  will be set to 1, and this will cause the  $i$ th agent to transit to GFM operation mode while other agents operate in GFL. This ensures at least one agent operates in GFM at any instance.

#### IV. SIMULATION CASE STUDIES AND DISCUSSION

To illustrate the efficacy of the proposed autonomous controller, three case scenarios have been investigated in MATLAB Simulink environment with five DERs connected to the PCC and feeding their local loads in an islanded PEDG cluster. The islanded PEDG cluster consists of one GFM inverter and four GFL inverters. System specifications for GFM and GFL inverters are provided in Table II.

- 1) Case Study 1 demonstrates the undesirable operation of the PEDG in the absence of the proposed control.
- 2) Case Study 2 illustrates the efficiency of the proposed SR-CMS mechanism in the restoration of PCC  $V-f$  without the proposed SC-based frequency restoration.
- 3) Case Study 3 illustrates the proposed autonomous control's ability to timely restore the frequency by dynamically assigning new set-points to the GFL inverter when a GFM inverter is faulted and a steep fluctuation in loading occurs.

##### A. Case Study 1: Operation in the Absence of the Proposed Control Scheme

Case study 1 illustrates a system of one droop-based GFM inverter and several GFL inverters operating in the absence of the proposed SR-CMS control scheme. The cluster comprises five DERs, with DER<sub>1</sub> operating in GFM and maintaining the

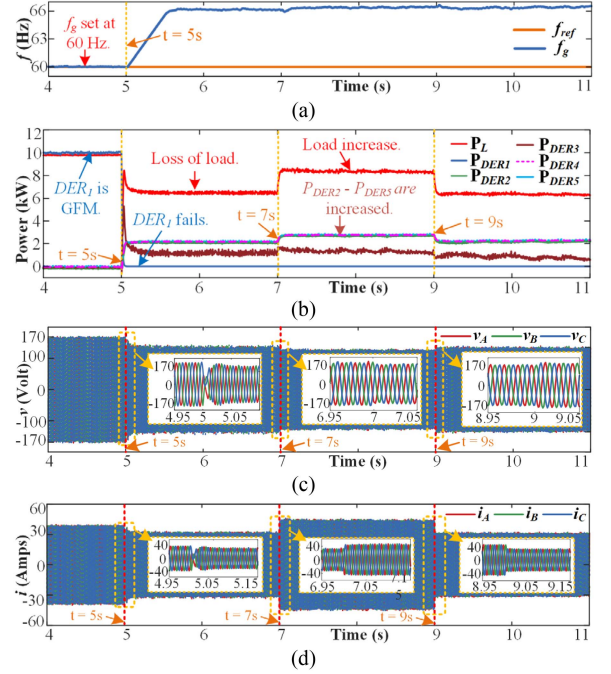


Fig. 6. Case study 1: GFM in conventional PEDG fails at  $t = 5$  s followed by step loading. (a) Frequency. (b) Active powers. (c) PCC voltages. (d) Load current. Violation of grid voltage/frequency bounds.

PCC  $V-f$ , whereas the other inverters are operating in GFL. Initially, all the DERs are feeding their local loads, and DER<sub>1</sub> regulates the frequency to 60 Hz, as shown in Fig. 6(a), while feeding the system load of 11.5 kW in Fig. 6(b). In the absence of the proposed control scheme, PEDG is highly susceptible to intentional and unintentional disturbances due to steep load variations or other potential anomalies or failures.

At  $t = 5$  s, the DER<sub>1</sub> controller fails. At this instance,  $P_{DER1}$  instantly drops to 0 W and the load power ( $P_L$ ) drops as well, indicating an undesirable loss of load. The frequency regulation is lost as it deviates to about 66 Hz [see Fig. 6(a)]. Moreover, the PCC voltage drops below the nominal value after  $t = 5$  s in Fig. 6(c). Under such conditions, system loading is varied by 5 kW between  $t = 7$  s and  $t = 9$  s. This causes the PCC voltage to further drop below the nominal value, as shown in Fig. 6(c). The load current also varies proportionately in Fig. 6(d). However, in this case study, a clear violation of  $V-f$  limits is observed, which would trigger relays and disconnect the inverters from the network.

##### B. Case Study 2: Validation of the Proposed Control Without SC

To ensure that the PCC voltage is regulated and uninterrupted power is always fed to loads, the proposed SR-CMS mechanism has been deployed in the PEDG network. Initially, DER<sub>1</sub> is assigned the GFM role, considering its highest initial priority of 0.9. DER<sub>2</sub> to DER<sub>5</sub> are regulated in GFL mode. For simplicity in explanation, the time duration is divided into five intervals ( $t_1-t_5$ ), as shown in the results in Fig. 7(a)–(f).



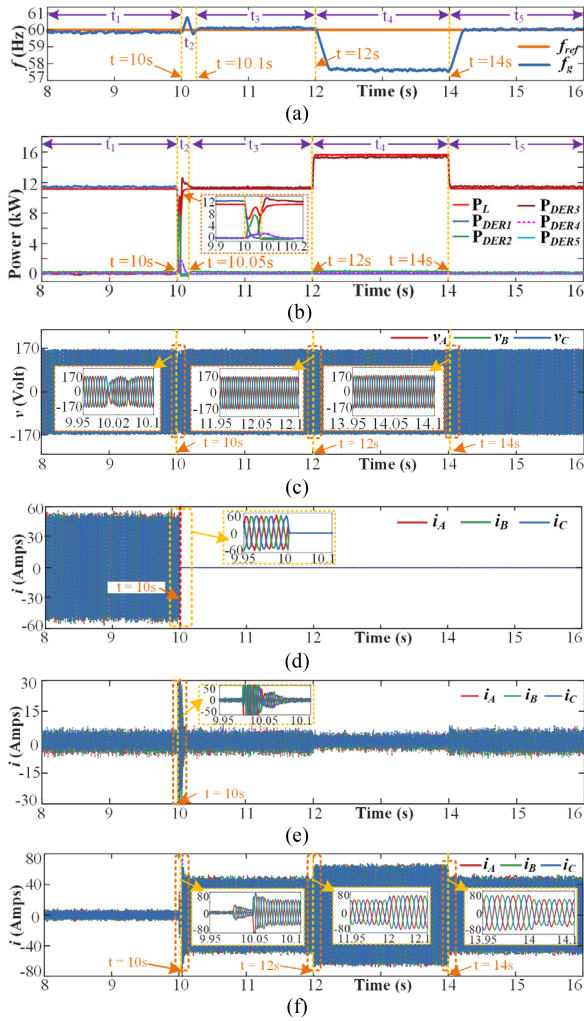


**Fig. 7.** Case study 2: faulted GFM  $DER_1$  at  $t = 10$  s and  $DER_2$  at  $t = 10.1$  s: (a) frequency, (b) active powers, (c) PCC voltage, (d)  $DER_1$  output current, (e)  $DER_2$  output current, and (f)  $DER_3$  output currents illustrating transition of GFM role from  $DER_1 \rightarrow DER_2 \rightarrow DER_3$  followed by load disturbances.

Initially, the system is stable in time interval  $t_1$ , and the frequency is maintained at 60 Hz, as shown in Fig. 7(a).  $DER_1$  feeds the 11.5 kW system load [blue plot in Fig. 7(b)], whereas  $DER_2$  to  $DER_5$  are synchronized with PCC voltage [see Fig. 7(c)]. Their power injection ( $P_{DER2}$  to  $P_{DER5}$ ) into the PEDG during the  $t_1$  interval is 0 W. At  $t = 10$  s, the GFM  $DER_1$  fails, as indicated by  $P_{DER1}$  [blue plot in Fig. 7(b)] dropping to 0 W and its output current falling to 0 A in Fig. 7(d). As the fault detection module detects a violation of PCC  $V-f$ , the SR-CMS mechanism triggers a fault, and  $DER_2$  with the next highest initial priority is elected as the next GFM in  $t_2$ .  $DER_2$  switches the mode to GFM and starts regulating the PCC's  $V-f$ . It also serves the load that was previously served by  $DER_1$ . This is evident from the brown plot in the zoomed window of Fig. 7(b). A proportionate increase in the  $DER_2$  output currents is observed in Fig. 7(e) in  $t_2$ . However, due to insufficient instantaneous available power,  $DER_2$  cannot meet the load requirements and hence fails ( $P_{DER2} \rightarrow 0$  W) at about  $t = 10.1$  s. Instantly, the SR-CMS mechanism

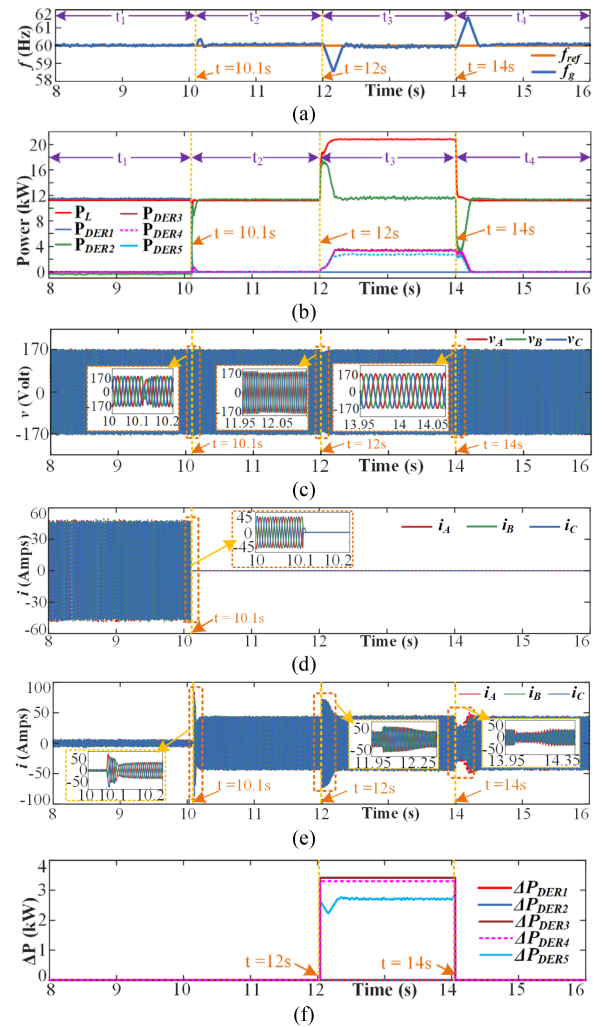


**Fig. 8.** Case Study 3: faulted GFM at  $t = 10.1$  s and load disturbances between  $t = 12$  s and  $t = 14$  s: (a) frequency, (b) active powers, (c) PCC voltages, (d)  $DER_1$  output currents (e)  $DER_2$  output currents, and (f) real-time  $\Delta P$  allocations for the timely restoration of PCC  $V-f$  for stable system operation due to the proposed autonomous control scheme with SC.

re-elects  $DER_3$  as the next GFM at the start of  $t_3$ .  $DER_3$ 's output currents also increase, as shown in Fig. 7(f).

Next, a step increase of 5 kW in system load is introduced at time instance  $t_4$  from  $t = 12$  s to  $t = 14$  s.  $DER_3$  increases its output power  $P_{DER3}$  [brown plot in  $t_4$  in Fig. 7(b)]. However, this causes the frequency to deviate to 59 Hz. Thus, frequency bounds could be violated, leading to undesirable operations.

### C. Case Study 3: Validation of the Proposed Autonomous Control Scheme With the SC

To ensure the real-time mitigation of frequency excursions during an event, the proposed SC Droop-OPA-based frequency restoration in the proposed autonomous control is incorporated. This ability of the proposed control to timely restore frequency is demonstrated here. The performance of the system in response to a failed GFM inverter followed by load disturbances is illustrated in Fig. 8(a)–(f).

Initially, during interval  $t_1$ , the frequency is held at 60 Hz [see Fig. 8(a)], and DER<sub>1</sub> supports the 11.5-kW system load [see Fig. 8(b)]. At  $t = 10.1$  s, the GFM operating DER<sub>1</sub> fails and is replaced by DER<sub>2</sub> as the next GFM by the SR-CMS mechanism. Thus,  $P_{\text{DER}_2}$  indicated by the green plot increases in interval  $t_2$  in Fig. 8(b). The PCC voltage remains almost uninterrupted, as shown in Fig. 8(c), whereas the collapse of DER<sub>1</sub> and rise of DER<sub>2</sub> power are also evident from their respective output currents in Fig. 8(d) and (e). At  $t = 12$  s, the system load is increased by 10 kW to simulate steep load fluctuations.

Initially, GFM DER<sub>2</sub> feeds this additional load by increasing its power output. This leads to a drift in the frequency, as can be seen in interval  $t_3$  in Fig. 8(a). This drift in frequency is detected by SC, and it increases the power allocations  $\Delta P$  to all GFL operating DERs [in Fig. 8(f)], to serve the additional load. This is evident from the rise in  $P_{\text{DER}_3}$ ,  $P_{\text{DER}_4}$ , and  $P_{\text{DER}_5}$  during the  $t_3$  interval in Fig. 8(b). Consequently,  $P_{\text{DER}_2}$  decreases almost immediately, and the frequency is returned to nominal 60 Hz in a timely manner (in less than 0.15 s), thereby satisfying the timing norms set by the grid standards. A similar type of fast frequency restoration is seen at the end of instance  $t_4$  when the system loading is decreased back to 11.5 kW.

Thus, the proposed autonomous control can maintain stable operation of the PEDG while mitigating the impacts of faulted GFM inverters as well as other disturbances related to system loading.

## V. EXPERIMENTAL VALIDATION

The proposed autonomous control scheme is validated experimentally on a system of three inverters representing a small-scale network of GFM and GFL DERs, as shown in Fig. 9(a). The connection topology of the three DERs is shown in Fig. 9(b). The primary- and secondary-level controllers for DER<sub>1</sub> and DER<sub>2</sub> were implemented on a dSPACE MicroLab box, whereas the primary- and secondary-level controllers for DER<sub>3</sub> and the proposed SC (consisting of  $\Delta P$  estimator and OPA module) were implemented on a Typhoon HIL 604. The power allocation set-points for DER<sub>1</sub>, DER<sub>2</sub>, and DER<sub>3</sub> are estimated by the SC implemented in Typhoon HIL 604 and are communicated through serial communication between the Typhoon 604 and the dSPACE. Each DER is equipped with an LCL filter, whose component values are provided in Table II. Programmable dc supplies are used to simulate the hybrid dc sources. Initially, DER<sub>1</sub> is regulated in the GFM mode, serving a system load of 50  $\Omega$ , whereas DER<sub>2</sub> and DER<sub>3</sub> operate in the GFL mode, serving their local loads of 22  $\Omega$  each, and are also connected to the DER<sub>1</sub> via the PCC contactor switches.

The line frequency is plotted in Fig. 10(a), and the output power profiles of each DER for the entire duration of the hardware testing are shown in Fig. 10(b). Furthermore, in the oscilloscope image in Fig. 10(c), the PCC voltage phase-a is represented by the yellow plot, whereas the phase-a currents of DER<sub>1</sub>, DER<sub>2</sub>, and DER<sub>3</sub> are represented by the red, green, and blue plots, respectively. Finally, the three-phase PCC voltage is shown by the red, blue, and yellow plots, whereas the DER<sub>2</sub> phase-a current is shown in Fig. 10(d). At  $t = 9.2$  s, the GFM

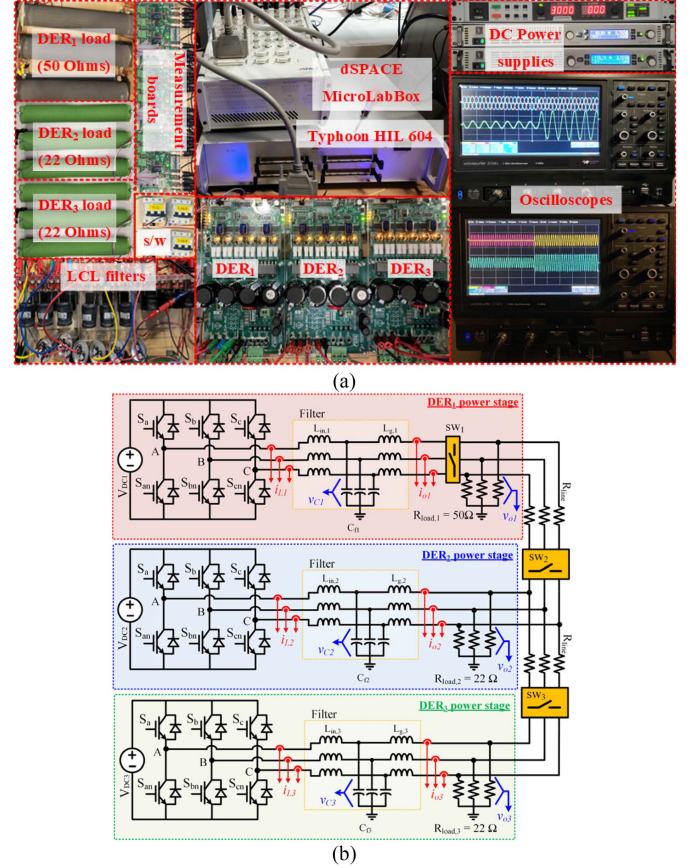
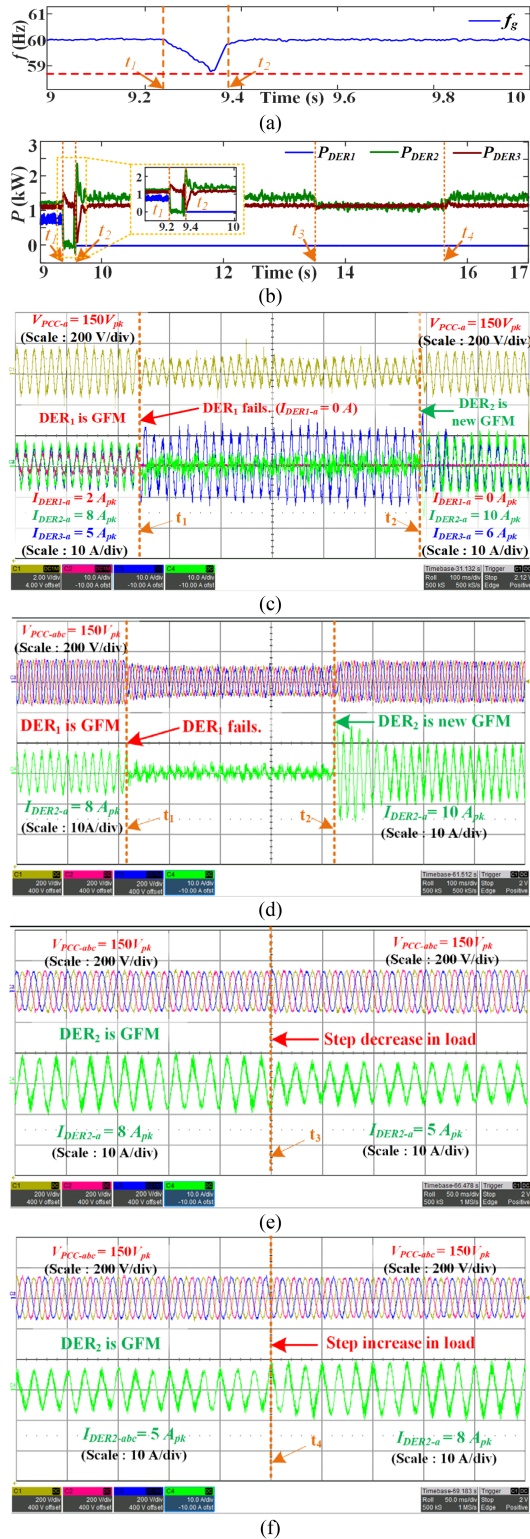


Fig. 9. (a) Experimental hardware setup of three DERs and (b) their connection topology in the microgrid testbed.

operating DER<sub>1</sub> is lost due to an intentional failure to represent the scenario of the loss of a GFM inverter. Thus, frequency and voltage regulation are lost, and frequency starts dropping from the nominal 60 Hz after time instance  $t_1$ , as observed in Fig. 10(a). After the DER<sub>1</sub> is lost, its output power drops to zero after time instance  $t_1$ , represented by the blue plot in Fig. 10(b). This can also be verified from the DER<sub>1</sub>'s phase-a current dropping to 0 Amps after time instance  $t_1$  [represented by the red plot in Fig. 10(c)]. Also, the three-phase PCC voltages in Fig. 10(d) drop below the nominal after  $t_1$ . This violation of PCC  $V$ - $f$  is detected by the fault detection modules in the secondary controllers of DERs. Furthermore, the fault status is also communicated to the secondary controllers of each DER internally. In the transition window between time instances  $t_1$  and  $t_2$ , the DER<sub>2</sub> is switching its operation mode from GFL to GFM. As shown in the post-fault period, the PCC voltage is not being regulated momentarily. This also causes the DER<sub>2</sub> currents to be unregulated [green plot in Fig. 10(c) and (d)].

As the fault is verified by the DER<sub>1</sub>'s secondary controller, it sets its local priority to 0 to indicate its inability to serve as the next GFM. After confirmation of the fault status, the DER<sub>2</sub>'s secondary control elects itself as the next GFM inverter, whereas the DER<sub>3</sub>'s controller continues to operate in the GFL mode based on the proposed SR-CMS scheme. Consequently, the DER<sub>2</sub>'s secondary control switches its operation mode from





**Fig. 10.** Experimental results: DER<sub>1</sub>, DER<sub>2</sub>, and DER<sub>3</sub> connected at PCC, where DER<sub>1</sub> is faulted and removed from the network at  $t = 9.2$  s. (a) Frequency. (b) Power profiles. (c) PCC phase-a voltage and phase-a currents of all three DERs when DER<sub>1</sub> is lost and DER<sub>2</sub> transitions to GFM between  $t_1$  and  $t_2$ . (d) Three-phase PCC voltages and DER<sub>2</sub> phase-a current when DER<sub>1</sub> is lost and DER<sub>2</sub>'s mode transition from GFL to GFM in about 0.4 s between  $t_1$  and  $t_2$ . (e) Step decrease in system load and (f) step increase in system load where PCC  $V$ - $f$  is maintained at their nominal values by newly elected GFM DER<sub>2</sub>.

GFL to GFM smoothly in less than 250 ms after the PCC  $V$ - $f$  limit violation is detected. The DER<sub>2</sub> now starts regulating the PCC  $V$ - $f$  after time instance  $t_2$ . This can be validated by the PCC voltage magnitude returning to nominal after time instance  $t_2$  in the oscilloscope waveforms shown in Fig. 10(c) and (d). Also, the line frequency is returned to the nominal 60 Hz in about 250 ms by the newly elected GFM DER<sub>2</sub>. This validates the operation of the proposed SR-CMS control scheme on a small-scale hardware setup. The DER<sub>2</sub>'s output current phase-a [green plot in Fig. 10(c) and (d)] also increases proportionately due to the overall increase in its load from  $22 \Omega$  to  $15.28 \Omega$ .

Next, to verify the operation of the DER<sub>2</sub> as the newly appointed GFM, the system load of  $30 \Omega$  is disconnected from the PCC at instance  $t_3$ . Thus, the load served by DER<sub>2</sub> drops to  $22 \Omega$ . It can be observed that the three-phase PCC voltage [red, blue, and yellow plots in Fig. 10(e)] is maintained at the nominal even after the load disturbance occurred at time instance  $t_3$ , whereas the DER<sub>2</sub>'s output current [green plots in Fig. 10(e)] decreases proportionately. Similarly, the GFM operating DER<sub>2</sub> regulates the PCC voltage to the nominal value [red, blue, and yellow plots in Fig. 10(f)] while its output current increases proportionately after time instance  $t_4$ , when the  $22 \Omega$  load is reconnected at the PCC. Thus, the GFM operation of DER<sub>2</sub> after the mode transition is verified. These results verify the functionality of the proposed autonomous control scheme with the frequency restoration in a small-scale hardware testbed.

## VI. CONCLUSION

An autonomous resilient control with SR-CMS and  $V$ - $f$  restoration capabilities for a cluster of inverters in a PEDG was proposed. During load disturbances, the OPA-based SC was capable of restoring frequency within the allowable time bounds. The droop-based  $\Delta P$  estimator accurately estimated the differential power required to restore the frequency, while the OPA module minimized the incurred power losses while ensuring timely restoration of the frequency. Moreover, the use of SC eliminated the dependency on the droop-based complex coordination to attain power sharing among interconnected inverters. Furthermore, the proposed SR-CMS mechanism enabled the instantaneous restoration of the PCC  $V$ - $f$  when a GFM inverter's controller was faulted or compromised. The case studies and results validated the ability and robustness of the proposed scheme to withstand during an event. Furthermore, the experimental results obtained from hardware testing on the small-scale testbed validated the feasibility of the proposed control scheme. Thus, the proposed control scheme enhanced the resiliency of the network of GFL and GFM inverters in PEDG.

*Disclaimer:* The statements made herein are solely the responsibility of the authors.

## REFERENCES

- [1] A. Khan, M. Hosseinzadehtaher, M. B. Shadmand, S. Bayhan, and H. Abu-Rub, "On the stability of the power electronics-dominated grid: A



- new energy paradigm,” *IEEE Ind. Electron. Mag.*, vol. 14, no. 4, pp. 65–78, Dec. 2020.
- [2] Y. Lin et al., “Research roadmap on grid-forming inverters,” Nat. Renewable Energy Lab. (NREL), Golden, CO, USA, Tech. Rep., NREL/TP-5D00-73476, 2020.
  - [3] S. D’silva, M. Shadmand, S. Bayhan, and H. Abu-Rub, “Towards grid of microgrids: Seamless transition between grid-connected and islanded modes of operation,” *IEEE Open J. Ind. Electron. Soc.*, vol. 1, pp. 66–81, Apr. 2020, doi: [10.1109/OJIES.2020.2988618](https://doi.org/10.1109/OJIES.2020.2988618).
  - [4] M. E. T. Souza and L. C. G. Freitas, “Grid-connected and seamless transition modes for microgrids: An overview of control methods, operation elements, and general requirements,” *IEEE Access*, vol. 10, pp. 97802–97834, Sep. 2022, doi: [10.1109/ACCESS.2022.3206362](https://doi.org/10.1109/ACCESS.2022.3206362).
  - [5] B. K. Poolla, D. Groß, and F. Dörfler, “Placement and implementation of grid-forming and grid-following virtual inertia and fast frequency response,” *IEEE Trans. Power Syst.*, vol. 34, no. 4, pp. 3035–3046, Jul. 2019.
  - [6] R. H. Lasseter, Z. Chen, and D. Pattabiraman, “Grid-forming inverters: A critical asset for the power grid,” *IEEE J. Emerg. Sel. Topics Power Electron.*, vol. 8, no. 2, pp. 925–935, Jun. 2020.
  - [7] J. Wang and G. Saraswat, “Study of inverter control strategies on the stability of low-inertia microgrid systems,” National Renewable Energy Lab. (NREL), Golden, CO, USA, Tech Rep. NREL/CP-5D00-81403, 2022.
  - [8] Y. Qi, H. Deng, J. Fang, and Y. Tang, “Synchronization stability analysis of grid-forming inverter: A black box methodology,” *IEEE Trans. Ind. Electron.*, vol. 69, no. 12, pp. 13069–13078, Dec. 2022.
  - [9] D. Y. Yamashita, I. Vecchiu, and J.-P. Gaubert, “A review of hierarchical control for building microgrids,” *Renewable Sustain. Energy Rev.*, vol. 118, 2020, Art. no. 109523.
  - [10] T. Khalili and A. Bidram, “Distributed control approaches for microgrids,” in *Microgrids*. Berlin, Germany: Springer, 2021, pp. 275–288.
  - [11] H. S. Bidgoli and T. Van Cutsem, “Combined local and centralized voltage control in active distribution networks,” *IEEE Trans. Power Syst.*, vol. 33, no. 2, pp. 1374–1384, Mar. 2018.
  - [12] C. Samende, S. M. Bhagavathy, and M. McCulloch, “Power loss minimization of off-grid solar DC nano-grids—Part I: Centralized control algorithm,” *IEEE Trans. Smart Grid*, vol. 12, no. 6, pp. 4715–4725, Nov. 2021.
  - [13] A. Singhal, T. L. Vu, and W. Du, “Consensus control for coordinating grid-forming and grid-following inverters in microgrids,” *IEEE Trans. Smart Grid*, vol. 13, no. 5, pp. 4123–4133, Sep. 2022.
  - [14] S. M. Mohiuddin and J. Qi, “Optimal distributed control of AC microgrids with coordinated voltage regulation and reactive power sharing,” *IEEE Trans. Smart Grid*, vol. 13, no. 3, pp. 1789–1800, May 2022.
  - [15] M. Chamana, B. H. Chowdhury, and F. Jahanbakhsh, “Distributed control of voltage regulating devices in the presence of high PV penetration to mitigate ramp-rate issues,” *IEEE Trans. Smart Grid*, vol. 9, no. 2, pp. 1086–1095, Mar. 2018.
  - [16] M. Bell, F. Berkel, and S. Liu, “Real-time distributed control of low-voltage grids with dynamic optimal power dispatch of renewable energy sources,” *IEEE Trans. Sustain. Energy*, vol. 10, no. 1, pp. 417–425, Jan. 2019.
  - [17] T. V. Vu, S. Paran, F. Diaz-Franco, T. El-Mezyani, and C. S. Edrington, “An alternative distributed control architecture for improvement in the transient response of DC microgrids,” *IEEE Trans. Ind. Electron.*, vol. 64, no. 1, pp. 574–584, Jan. 2017.
  - [18] X. Li, D. Hui, and X. Lai, “Battery energy storage station (BESS)-based smoothing control of photovoltaic (PV) and wind power generation fluctuations,” *IEEE Trans. Sustain. Energy*, vol. 4, no. 2, pp. 464–473, Apr. 2013.
  - [19] D. Curto et al., “Grid stability improvement using synthetic inertia by battery energy storage systems in small islands,” *Energy*, vol. 254, 2022, Art. no. 124456.
  - [20] U. Markovic, O. Stanojev, P. Aristidou, and G. Hug, “Partial grid forming concept for 100% inverter-based transmission systems,” in *Proc. IEEE Power Energy Soc. Gen. Meeting*, 2018, pp. 1–5.
  - [21] J. W. Simpson-Porco, Q. Shafiq, F. Dörfler, J. C. Vasquez, J. M. Guerrero, and F. Bullo, “Secondary frequency and voltage control of islanded microgrids via distributed averaging,” *IEEE Trans. Ind. Electron.*, vol. 62, no. 11, pp. 7025–7038, Nov. 2015.
  - [22] M. Eskandari, L. Li, M. H. Moradi, P. Siano, and F. Blaabjerg, “Active power sharing and frequency restoration in an autonomous networked microgrid,” *IEEE Trans. Power Syst.*, vol. 34, no. 6, pp. 4706–4717, Nov. 2019.
  - [23] H. Han, X. Hou, J. Yang, J. Wu, M. Su, and J. M. Guerrero, “Review of power sharing control strategies for islanding operation of AC microgrids,” *IEEE Trans. Smart Grid*, vol. 7, no. 1, pp. 200–215, Jan. 2016.
  - [24] S. D’Silva, M. Hosseinzadehtaher, M. B. Shadmand, S. Bayhan, H. Abu-Rub, and T. Huang, “Coordinated power reserve control of PV sources for frequency restoration in power electronics dominated grid,” in *Proc. IEEE 3rd Int. Conf. Smart Grid Renewable Energy*, 2022, pp. 1–7.
  - [25] R. Guzman, L. G. de Vicuña, A. Camacho, J. Miret, and J. M. Rey, “Receding-horizon model-predictive control for a three-phase VSI with an LCL filter,” *IEEE Trans. Ind. Electron.*, vol. 66, no. 9, pp. 6671–6680, Sep. 2019.
  - [26] K.-W. Lao, W. Deng, J. Sheng, and N. Dai, “PQ-coupling strategy for droop control in grid-connected capacitive-coupled inverter,” *IEEE Access*, vol. 7, pp. 31663–31671, Mar. 2019, doi: [10.1109/ACCESS.2019.2902314](https://doi.org/10.1109/ACCESS.2019.2902314).



**Silvanus D'silva** (Student Member, IEEE) received the bachelor's degree in electronics and telecommunication engineering from the University of Mumbai, Mumbai, India, in 2014, and the M.Sc. degree in electrical engineering from Kansas State University, Manhattan, KS, USA, in 2020. He is currently working toward the Ph.D. degree in electrical engineering at the University of Illinois Chicago, Chicago, IL, USA.

From January 2021 to August 2021, he was a graduate researcher with the TEES Lab, Smart Grid Centre, Texas A&M University at Qatar, Doha, Qatar. In August 2021, he joined the IPEG Research Group.



**Alireza Zare** (Student Member, IEEE) received the B.Sc. degree in electrical engineering with a focus on power engineering from Shiraz University, Shiraz, Iran, in 2017, and the M.S. degree in electrical and electronics engineering from Washington State University, Vancouver, WA, USA, in 2020. He is currently working toward the Ph.D. degree in electrical engineering in the Electrical and Computer Engineering Department, University of Illinois Chicago, Chicago, IL, USA.



**Mohammad B. Shadmand** (Senior Member, IEEE) received the Ph.D. degree in electrical engineering from Texas A&M University, College Station, TX, USA, in 2015.

From 2017 to 2020, he was an Assistant Professor with the Department of Electrical and Computer Engineering, Kansas State University, Manhattan, KS, USA. Since 2020, he has been an Assistant Professor with the University of Illinois Chicago, Chicago, IL, USA.

Dr. Shadmand was the recipient of the Michelle Munson Serban Simu Keystone Research Scholar Award, Kansas State University, in 2017 and the 2019 IEEE Myron Zucker Faculty-Student Research Grant. He was also the recipient of multiple best paper awards at different IEEE conferences. He is the General Co-Chair of the 50th Annual Conference of the IEEE Industrial Electronics Society (IECON 2024), Chicago, IL, USA. He is an Associate Editor for the IEEE TRANSACTIONS ON INDUSTRIAL ELECTRONICS, the IEEE TRANSACTIONS ON INDUSTRY APPLICATION, and *IET Renewable Power Generation*.



**Sertac Bayhan** (Senior Member, IEEE) received the bachelor's, M.S., and Ph.D. degrees in electrical engineering from Gazi University, Ankara, Turkey, in 2008 and 2012, respectively.

He is currently a Senior Scientist with the Qatar Environment and Energy Research Institute, Hamad Bin Khalifa University, Doha, Qatar, where he is a Faculty Member with the rank of an Associate Professor with the Sustainable Division, College of Science and Engineering.

He has acquired \$13M in research funding and published more than 170 papers in mostly prestigious IEEE journals and conferences. He has coauthored two books and five book chapters.

Dr. Bayhan was the recipient of many prestigious international awards.



**Haitham Abu-Rub** (Fellow, IEEE) received the two Ph.D. degrees, one in electrical engineering from the Technical University of Gdansk, Gdansk, Poland, in 1995, and one in the humanities from Gdansk University, Gdansk, Poland, in 2004.

He has research and teaching experiences at many universities in many countries, including Poland, Palestine, USA, Germany, and Qatar. Since 2006, he has been with Texas A&M University at Qatar, Doha, Qatar. For five years, he was the Chair for the Electrical and Computer Engineering Program, Texas A&M University at Qatar. He is currently the Managing Director of the Smart Grid Center. He has authored or coauthored more than 400 journal articles and conference papers, five books, and six book chapters. He has supervised many research projects on smart grids, power electronics converters, and renewable energy systems. His main research interests include electric drives, power electronic converters, renewable energy, and smart grids.

Dr. Abu-Rub was the recipient of many national and international awards and recognitions. He was the recipient of the American Fulbright Scholarship, the German Alexander von Humboldt Fellowship, and many others.